Ambient ozone pollution at a coal chemical industry city in the border of Loess Plateau and Mu Us Desert: characteristics, sensitivity analysis and control strategies

Manfei Yin[1,2], Xin Zhang[2,3], Yunfeng Li[2,3], Kai Fan[4], Hong Li[2], Rui Gao[2] and Jinjuan Li[1]

[1] College of Resource and Environment Engineering, Guizhou University, Guiyang, China
[2] State Key Laboratory of Environmental Criteria and Risk Assessment, Chinese Research Academy of Environmental Sciences, Beijing, China
[3] Environment Research Institute, Shandong University, Jinan, China
[4] Yulin Municipal Ecology and Environment Bureau, Yulin, China

ABSTRACT

In this study, ambient ozone (O_3) pollution characteristics and sensitivity analysis were carried out in Yulin, a city in the central area of the Loess Plateau during 2017 to 2019 summer. O_3 concentrations increased for 2017 to 2019. Correlation and statistics analysis indicated high temperature (T > 25 °C, low relative humidity (RH < 60%), and low wind speed (WS < 3 m/s) were favorable for O_3 formation and accumulation, and the O_3 pollution days (MDA8 O_3 > 160 μg/m³) were predominantly observed when the wind was traveling from the easterly and southerly. O_3 concentration in urban area of Yulin was higher than that in background. The pollution air masses from Fenwei Plain increase the level and duration of O_3 pollution. In order to clarify the formation mechanism and source of O_3, online measurements of volatile organic compounds (VOCs) were conducted from 7 July to 10 August in 2019. The average of VOCs concentration was 26 ± 12 ppbv, and large amounts of alkenes followed by aromatics, characteristic pollutants of the coal chemical industry, were detected in the ambient air. To further measure the sensitivity, the observation-based model (OBM) simulation was conducted. Empirical Kinetic Modeling Approach (EKMA) plot and relative incremental reactivity (RIR) value indicated Yulin located on VOCs-limited regime. That implied a slight decrease of NO_x may increase O_3 concentration. When the emission reduction ratio of anthropogenic VOCs/NO_x higher than 1:1, the O_3 will decrease. O_3 control strategies analysis shows that the O_3 targets of 5% and 10% O_3 concentration reductions are achievable through precursor control, but more effort is needed to reach the 30% and 40% reduction control targets.

Subjects Atmospheric Chemistry, Environmental Impacts
Keywords Ozone, Sensitivity, Coal chemistry, Loess Plateau, Characteristics, OBM simulation

INTRODUCTION

China's ozone (O_3) concentrations have shown a gradual upward trend over recent years. Studies on China's O_3 pollution in China have focused on more developed regions, such as Beijing-Tianjin-Hebei (BTH) (*Duan et al., 2008*; *Xu et al., 2011*; *Zhang et al., 2014b*; *Yan et al., 2016b*), the Yangtze River Delta (YRD) (*Wang et al., 2020b*; *Zhang et al., 2020b*), the Pearl River Delta (PRD) (*Chen et al., 2019*; *He et al., 2019*), and the Guanzhong Plain (GZP) (*Hui et al., 2021*), which is close to the Loess Plateau. However, few studies have been conducted on the Loess Plateau itself (*Li et al., 2020a*; *Li et al., 2020b*; *Wang et al., 2012*). The Loess Plateau is to the north of central China, and is one of the country's four major plateaus. Since much of its arid surface is exposed, it becomes a source of suspended particulate matter (PM) that pollutes cities in north China during dry and windy weather (*Cao et al., 2008a*). China began carrying out vegetation rehabilitation programs in 1978 (*Li et al., 2017*). With stricter air pollution control and the increase of comprehensive studies on PM between 2014 and 2017 (*Cao et al., 2008a*; *Cao et al., 2008b*; *Liu et al., 2004*; *Wang et al., 2011*; *Zhang et al., 2014a*; *Xiaoye, 2002*), the $PM_{2.5}$ pollution problem plaguing Loess Plateau, and many other parts of China (*Cao et al., 2012*; *Zhang et al., 2019*), has been effectively alleviated, while O_3 concentrations continue to rise. O_3 has become the primary pollutant affecting Loess Plateau's ambient air quality in the summer.

Yulin (38.25N, 109.73E) is located in the central area of Loess Plateau, in the northernmost part of Shaanxi Province (*Zhu et al., 2019*). It is in the junction area of Jin-Shan-Meng-Ning (Shanxi, Shaanxi, Inner Mongolian, and Ningxia provinces), which is one of China's five main coal production areas and one of the main battlefields for coal exploitation in China (*Hao et al., 2019*). Yulin is a typical energy resource city, with proven coal reserves of 2.7×10^3 billion tons. In 2019, the output of raw coal alone was 4.6×10^5 kilo-tons. The area's rapid development and energy advantages (*Zhai et al., 2020*) have caused many environmental problems. Previous research on this area mainly focused on PM. *Lei et al. (2018)* found that Yulin's high Ca^{2+} levels during winter and autumn are attributed to fugitive dust, while high spring and summer sulfate levels are caused by different sources. Ion balance studies illustrated that PM_{10} samples were more alkaline than $PM_{2.5}$ samples. *Wang et al. (2011)* found that dust aerosol invading Yulin could be from the northwestern desert in China and the Gobi Desert in Mongolia. CO and PM_{10} levels decreased while $PM_{2.5}$, O_3, and NO_2 levels increased (Fig. S1). $PM_{2.5}$ and O_3 were the primary pollutants in winter and summer, respectively. Very few studies have reported on this rise of O_3 concentrations (*Li et al., 2020a*; *Hou et al., 2006*). It is critical to explore the effect of local generation and transport on Yulin's O_3 levels.

In this paper, we analyzed the temporal and spatial characteristics of O_3 and the influence of meteorological factors from 2017–2019. We used the observation-based (OBM) model to study the sensitivity of O_3 formation to VOCs and NO_x between July and August 2019. Additionally, we set several targets in our discussion of O_3 control strategies.

MATERIALS & METHODS

Measurement data

To evaluate Yulin's O_3 characteristics between 2017 and 2019, we obtained observational hourly concentrations of air pollutants including O_3, CO, NO_2, PM_{10}, $PM_{2.5}$, and NO, as well as meteorological parameters including temperature (T), relative humidity (RH), wind speed (WS), and wind direction (WD) from National Environmental Monitoring Stations and the Yulin Ecology and Environment Bureau. In Yulin, we chose four stations for study: the Environmental Monitoring Building (EMB, 38.25°N, 109.73°E), Experimental Middle School (EMS, 38.28°N, 109.73°E), Century Square (CS, 38.29°N, 109.48°E), and Hongshixia Gorge Eco-Park (HGEP, 38.33°N, 109.74°E). The locations of the four stations are presented in Fig. 1. There are no significant local sources close to these four sites. Ambient Air Quality Monitoring Specification (on trial) *(Chinese HJ 664-2013)* classified the EMB site, EMS site, and CS site as urban assessing stations and the HGEP site as an urban background station. Urban assessing stations are set up to monitor ambient air quality and changing trends in urban built-up, and participate in the assessment of urban ambient air quality. Urban background stations monitor the ambient air quality in urban areas that are not affected by local urban pollution and do not participate in the assessment of urban ambient air quality. The EMB site is surrounded by a residential area and processing, manufacturing, and coal chemical industries are located about 5 km south. The EMS site and CS site are in mixed functional areas of commerce, transportation, and residences. Although the HGEP site is regulated as an urban background station, it was surrounded by a highway during our field survey and many trucks passed through it.

To investigate the characteristics of VOCs and their contribution to O_3 formation in Yulin, we coupled online gas chromatography with a mass spectrometer and a flame ionization detector (GC-MS/FID, AC-GCMS 1000) developed by Guangzhou Hexin Instrument Co., Ltd. This was used to measure VOC levels at the EMB site from 7 July to 10 August 2019. A total of 70 VOCs (18 alkanes, 11 alkenes, one ethyne, 16 halocarbons, 14 aromatics, and 10 oxygenated VOCs (OVOCs)) were measured concurrently with 1 h resolution. The air passed over two cold traps in the separate FID and MS routes, and samples were rapidly heated and vaporized at a rate of up to 50 °C/s. The VOCs were brought into the FID and MS for online qualitative and quantitative analysis, respectively. The C_2-C_4 hydrocarbons were analyzed by the FID and the high carbon components were analyzed by the MS. To check the stability of the monitoring system, we injected the mixed standard gas (Photochemical Assessment Monitoring Stations (PAMS)) and the US Environmental Protection Agency toxic organics (TO-15)) with a concentration of 1ppb into the system seven times, and calculated the relative standard deviation (RSD) of the concentration for each component. The results showed that the RSD of all VOCs was lower than 10% (Table S1). A seven-point calibration curve was made using the standard gas external standards with the linearity (R^2) of each VOC species exceeding 0.99. Another standard gas was injected daily into the instrument to test the system performance at 23:00. Therefore the data from 23:00 local time (LT) were excluded in this study.

Figure 1 Locations of four National Environmental Monitoring Stations (HGEP, CS, EMS and EMB). (Map data ©2020 Google Earth).

Backward trajectory analysis

The 48 h backward trajectories from May to August 2017 to 2019 were computed using the Hybrid Single-Particle Lagrangian Integrated Trajectory (HYSPLIT) model (*Cohen et al., 2015*; *Draxler & Hess, 1998*) with 6-h intervals and a start time of 00:00 LT to identify the origins of air masses 1,000 m above sea level. The meteorological data were provided by the Global Data Assimilation System of the United States National Centers for Environmental Prediction (ftp://arlftp.arlhq.noaa.gov/pub/archives/gdas1). These backward trajectories from 2017, 2018, and 2019 were analyzed using HYSPLIT, and then were categorized into a few clusters for analysis of the influence of O_3 regional transported sources.

Observational-based model

The OBM was developed by *Cardelino & Chameides (1995)* and was built on the newest version of the Master Chemical Mechanism (MCM v3.3.1; http://mcm.leeds.ac.uk/MCM/), a near-explicit mechanism describing the oxidation reactions of 146 primary VOCs together with the latest inorganic chemistry from the International Union of Pure and Applied Chemistry evaluation (*He et al., 2020*). Hourly concentrations of VOCs and four trace gases (SO_2, CO, NO, and NO_2), as well as hourly meteorological parameters (temperature and relative humidity), were used as inputs to constrain the model (*Lyu et al., 2019*). Moreover, this model can be employed to assess the sensitivity of O_3 photochemical production by calculating the relative incremental reactivity (RIR) and changing the concentrations of its precursors without detailed or accurate knowledge of these emissions (*He et al., 2019*):

$$RIR(X) = \frac{\left[P_{O_3}(X) - P_{O_3}(X - \Delta X)\right]/P_{O_3}(X)}{\Delta S(X)/S(X)}$$

where X is a precursor of O_3 and $\triangle X$ represents the change in X concentrations; $P(O_3)$ is the O_3 net production rate, which is calculated by the OBM; $S(X)$ is the measured concentration of precursor X, and $\triangle S(X)/S(X)$ represents the relative change of $S(X)$ (20% $S(X)$ in this study).

Positive matrix factorization model

The positive matrix factorization (PMF) model is used to interpret source types and contributions based on VOC concentrations obtained from receptor point measurements (*Paatero & Tapper, 1994*). It has been used for the source apportionment of VOCs (*Sun et al., 2020*). In this study, we used PMF 5.0 to identify and quantify the main VOC sources in Yulin. A detailed description of the PMF model can be found in the EPA PMF 5.0 User Guide. Briefly, the ambient VOC observations matrix (x) was decomposed into two matrices: source profile (f) and source contribution (g):

$$x_{ij} = \sum_{k=1}^{p} g_{ik}f_{kj} + e_{ij}$$

where, x_{ij} is the concentration of species j measured in sample i; g_{ik} is the contribution of the source k to the sample i; f_{kj} isthe profile of the species i in the source k; e_{ij} is the residual of species j in sample i; and p represents the total number of sources (*Fan et al., 2020*). In this study, we measured 70 VOC species and divided these species into three categories according to their signal-to-noise ratio (S/N) and detection limit (BDL). In general, species were classified as strong if the S/N was >2, weak if the S/N was between 0.2 and 2 or if the BDL percentage was >50%, and bad if the S/N was <0.2 or if the BDL percentage was >60% (*Hui et al., 2020*). Ultimately, 46 VOC species were selected and served as inputs of the PMF model.

In the PMF model, Q was the sum of the squared residual weighted by the inverse of their respective measurement uncertainty and in order to minimize the value. Q can be described as:

$$Q = \sum_{i=1}^{n} \sum_{j=1}^{m} \left(\frac{X_{ij} - \sum_{k=1}^{p} g_{ik}e_{kj}}{S_{ij}} \right)$$

Ideally, the modeled Q value should eventually approach the expected Q values (Q_{exp}), which are equal to the degree of freedom of the model solution (n ×m −p(n+m) (*Yan et al., 2016a*).

RESULTS

Temporal O_3 distribution characteristics

According to the Chinese Technical regulation for ambient air quality assessment (on trial) (*Chinese HJ 663-2013*), 1-hour average O_3 concentrations and daily maximum 8-hour average O_3 concentrations (MDA8) are employed to describe hourly and daily O_3 variations, respectively. The 90th percentile of daily maximum 8-h average of O_3 concentrations (MDA8-90) is employed to evaluate monthly and annual O_3 concentration levels. In this study, we used both MDA8 and maximum daily 1-hour average O_3

concentrations (MDA1) to present daily mean and extreme O_3 concentrations. The Ambient Air Quality Standard (*Chinese GB3095-2012*) regulates the Grade II Standard of MDA8 and MDA1 O_3, and are 160 μg/m^3 (about 75 ppbv) and 200 μg/m^3 (about 93 ppbv), respectively. We defined the day when MDA8 or MDA1 O_3 levels exceeded the Grade II Standard as O_3 pollution day. Moreover, we also evaluated the diurnal, monthly, and annual variations observed in Yulin. The HGEP site was an urban background station which, according to technical regulation for the selection of ambient air quality monitoring stations (on trial) in China, are not included in the evaluation of a city's air quality. Therefore, the HGEP site data were not included in the description of ambient O_3 changes in Yulin.

As shown in Table 1, the mean MDA8 O_3 concentration, MDA8-90 O_3 concentration, and pollution days all showed a rising trend from 2017 to 2019. Previous studies found that the average MDA8 O_3 concentration for China's 31 capital cities in 2013 and 2017 was 61 and 76 ppbv, respectively (*Zeng et al., 2019*). In the YRD, the average MDA8 O_3 concentration was 78 ppbv in 2018 (*Li et al., 2019*). In Lanzhou, China, the average MDA8 O_3 concentration from 2013 to 2015 was 68.26 μg/m^3 (about 32 ppbv) (*Wang et al., 2017b*). The average MDA8 O_3 concentration in the GZP was 96 μg/m^3 (about 45 ppbv) in 2019 (http://sthjt.shaanxi.gov.cn/zfxxgk/hjzl/hjzkgb/20201130/64307.html). Generally, O_3 concentrations in Yulin were lower than developed areas such as cities in the YRD, comparable to the national average level and the GZP, and higher than Lanzhou.

The O_3 pollution days all occurred between May and August in 2017 and 2018. One unanticipated finding was that O_3 pollution days also appeared in April and September in 2019. The T, RH, and WS averages in April and September 2019 were 15 °C and 19 °C, 43% and 65%, and 1.7 m/s and 1.3 m/s, respectively. The T, RH, and WS averages in April and September 2017 to 2019 were 14 °C and 18 °C, 41% and 61%, and 1.8 m/s and 1.5 m/s, respectively (Table S2). The meteorological conditions in April and September 2019 were not significantly different from those in 2017 and 2018. Two O_3 pollution days occurred consecutively from 18 to 19 April 2019. On 18 April, the O_3 concentration peaked at 19:00 LT, decreased to 51.3 ppbv the next day at 5:00, and then started to increase again. Relatively high O_3 concentration at night could be explained by regional transportation. Six consecutive O_3 pollution days occurred from 3 to 8 September 2019. Unlike the O_3 pollution days in April, regional transportation was not the primary reason for this O_3 pollution episode. The average NO_2 concentrations from 3 to 8 September were 20, 22, 27, 28, 22, and 21 ppbv, respectively, which were higher than the average concentrations on adjacent days, such as 2 September (16.6 ppbv) and 9 September (12.8 ppbv). This suggests that the continued increase in O_3 concentration may have been closely related to the increase in nitrogen dioxide concentration.

Figure 2A displays the monthly O_3 variations. The highest MDA8-90 O_3 concentrations in 2017, 2018, and 2019 were 40, 39, and 39 ppbv, respectively. The highest MDA8-90 O_3 concentration appeared in May 2017 and June 2019. MDA8-90 O_3 concentrations in May to July 2017-2019 exceeded the Grade II Standard. Additionally, the MDA8-90 O_3 concentration in April and September 2019 also exceeded the standard. Monthly O_3 variations reflected an obvious seasonal cycle, as O_3 concentrations were high in summer

Table 1 Mean daily maximum 8-h average (MDA8) O_3 concentrations, the 90th percentile of MDA8 O_3 (MDA8-90) concentrations and number of pollution days from 2017–2019.

Year	MDA8-90 O_3 (ppbv)	Mean MDA8 O_3 (ppbv)	Number of pollution days
2017	72	47 ± 18	26
2018	72	47 ± 19	25
2019	75	48 ± 19	34

and spring and low in winter and autumn. Some areas in north China also show this kind of seasonal cycle (*Fang et al., 2020*; *Yan et al., 2016b*; *Wang et al., 2012*; *Li et al., 2020a*). This seasonal O_3 variation was largely influenced by meteorological conditions (*Wang et al., 2020b*; *Zheng et al., 2019*).

The diurnal variation of O_3 concentrations is driven by photochemical reactions, meteorological conditions, the transport of O_3 and its precursors, and surface deposition (*Crutzen, 2016*; *David & Nair, 2011*). The diurnal variation in Yulin from 2017-2019, similar to many cities in northern China, shows a typical single peak curve: a valley in early morning and a peak in afternoon (Fig. 2B; *Wang et al., 2012*; *Yu et al., 2020b*; *Li et al., 2020a*). It was apparent that the O_3 concentrations were highest in summer, then spring, autumn, and winter. The O_3 concentration peaks were 60, 67, 43, and 34 ppbv in spring, summer, autumn, and winter, respectively. The peaks occurred at 16:00 LT in spring, autumn, and winter, but at 15:00 LT in summer. The solar radiation on Loess Plateau is intense, especially in summer, which can lead to more efficient O_3 production (*Hu et al., 2014*).

Spatial O_3 distribution characteristics

The four Yulin sites from most south to most north are the EMB, EMS, CS, and HGEP. Figure 3 shows that O_3 concentrations decreased spatially from south to north between 2017 and 2018. In 2017, the EMB site had the highest O_3 concentration, followed by the CS site, then the EMS site, and the HGEP site. In 2018, the O_3 concentrations decreased from south to north. In 2019, the EMB site had the highest O_3 concentration, followed by the HGEP site, then the EMS site, and the CS site, implying that the central region had lower O_3 concentrations than the northern and southern regions. The EMB site had the highest concentrations between 2017 and 2019. This suggested that Yulin's O_3 concentration was greatly affected by industry. Diurnal and monthly variations at the four sites showed the same trend (Fig. S2). The diurnal variation curve showed that the lowest concentrations appeared at 7:00 LT in the morning and the highest concentrations appeared at 16:00 LT in the afternoon. The distance between these sites is less than 5 km. Therefore, different pollution sources can explain the differences in O_3 concentrations at the four sites.

The HGEP site's O_3 concentration increased from 2017 to 2019 but was lower than that of Yulin's urban area. The monthly and daily changes were consistent with those of the urban area. However, the O_3 concentrations were lower at night at the HGEP site than at the other sites (Fig. S2A). As mentioned above, the HGEP site is a traffic-intensive area, and vehicles emit NO that can titrate and lower O_3 levels.
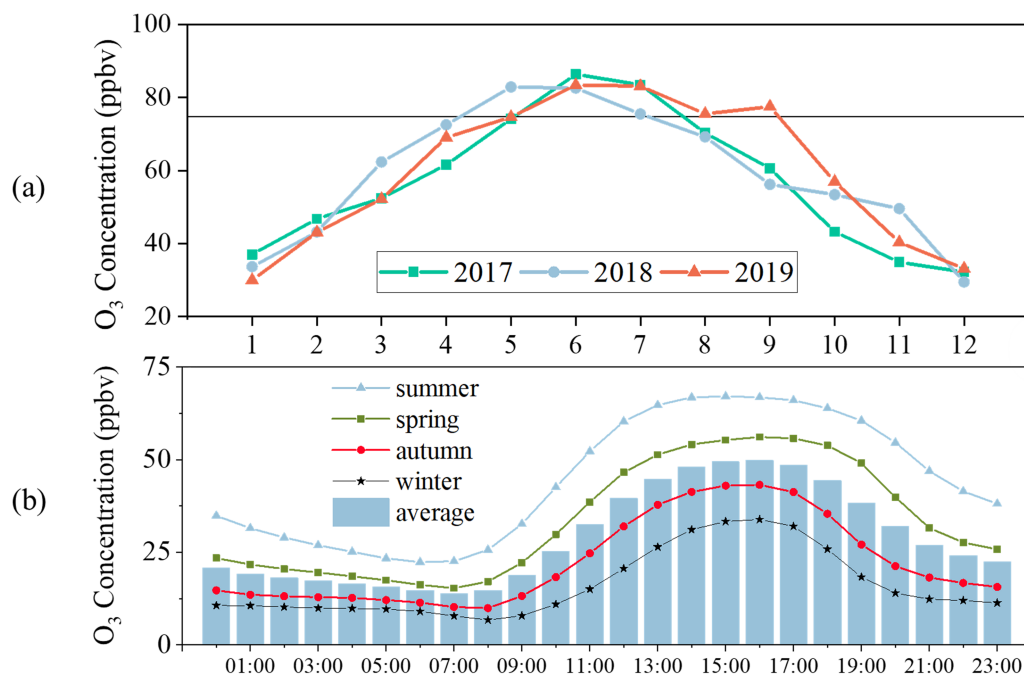
Figure 2 (A) Monthly variation of MDA8-90 O_3 concentrations, (B) diurnal variation of 1-hour average O_3 concentrations.
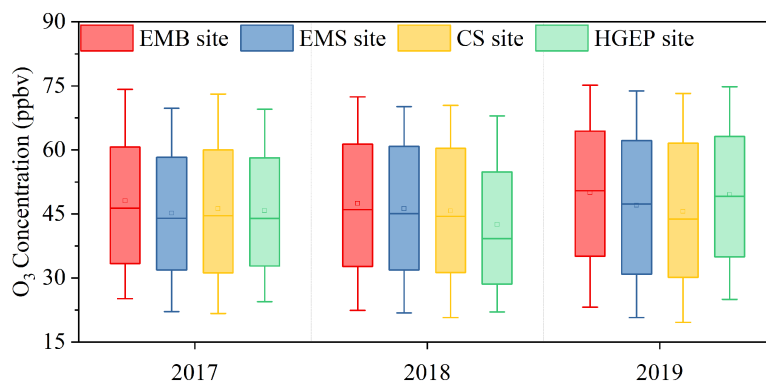
Figure 3 O_3 concentrations distributed at four sites in Yulin from 2017 to 2019. In each box plot, the block is the mean, the horizontal line crossing the box is the median, the bottom and top of the box are lower and upper quartiles, and the whiskers are the 10th percentile and 90th percentile.

Overview of O_3 pollution during the VOC sampling period

To further reveal the impact of O_3 local formation, we collected VOC samples at the EMB site from 7 July to 10 August 2019. Figure 4 shows the time series of the meteorological factors and NO_2, CO, $PM_{2.5}$, PM_{10}, VOC, and O_3 concentrations in Yulin during the VOC sampling period. The average values are listed in Table S3. We regarded consecutive MDA8 O_3 pollution days as one O_3 episode period (EP). There were a total of six O_3 episode periods (EP1: 11-14 July, EP2: 20 July, EP3: 25-26 July, EP4: 28 July, EP5: 30 July-2 August,

and EP6: 10 August) observed during the sampling period. During the sampling period, the average MDA8 O_3 concentration was 72 ± 9 ppbv with a range from 50 ppbv to 85 ppbv, and 83 ± 2, 75, 82 ± 3, 77, 79 ± 3 and 84 ppbv, respectively, from EP1 to EP6. The average concentration of total VOCs was 26 ± 12 ppbv with a wide range from 6 to 90 ppbv, and 30, 41, 28, 27, 31, and 13 ppbv, respectively, in the EPs. The meteorological factors of these six EPs (Table S3) were beneficial to in situ photochemical processes. NO_2 and total volatile organic compound (TVOC) concentrations were higher than in the non-pollution period. This indicated an increase in local precursor emissions. The valley values on 26 July (EP3), 28 July (EP4), 2 August (EP5), and 10 August (EP6) were 31, 22 50, and 33 ppbv, respectively. Compared to the average valley value during the VOC sampling period (19 ppbv) and the median value (16 ppbv), these valley values were relatively high. This result implied that EP3, EP4, EP5, and EP6 were also affected by regional transportation. The 48 h backward trajectories when hourly O_3 concentrations were over 75 ppbv are shown in Fig. S3. Most of the backward trajectories of EP1 and EP2 came from local and southwest areas, respectively, and there were no O_3 pollution areas along the trajectories. Most of the backward trajectories of EP3, EP4, and EP5 came from the Fenwei Plain, and O_3 pollution also occurred in the cities along the trajectories (Table S4). However, during EP6, no pollution was found along the trajectories. This O_3 EP was complex and the data cannot be explained. Determining whether the changes in O_3 concentration were caused by transportation, meteorological conditions, or anthropogenic sources will be our focus in future studies.

Different VOC species are capable of influencing O_3 formation potential (OFP), which can be estimated using Maximum Incremental Reactivity (MIR) (Carter, 2009). The OH reactivity concept is useful when estimating VOC O_3 production because VOC degradation caused by OH oxidation eventually leads to net O_3 production (Tan et al., 2018). OH reactivity is the sum of the products of precursor O_3 concentrations and the reaction rate constants between O_3 precursors and OH (Atkinson & Arey, 2004). The percentage contributions of alkanes, alkenes, ethyne, halocarbons, aromatics, oxygenated VOCs, and isoprene to the mixing ratio, L_{OH}, and OFP of total VOCs are shown in Fig. 5. Among these, alkanes were the most abundant VOC species, accounting for 46.2%, followed by OVOCs (26.9%), alkenes (10.1%), aromatics (7.8%), ethyne (4.3%), halocarbons (4.3%), and isoprene (0.4%). Although alkanes were the most abundant VOC species in Yulin, the proportions of L_{OH} (12.7%) and OFP (14.0%) were relatively small. Alkenes (31.8%), OVOCs (31.7%), and aromatics (21.3%) were the top three VOC species in terms of OFP proportion. L_{OH} and OFP showed good consistency, and alkenes (44%), OVOCs (23.5%), and aromatics (12.8%) had the top three proportions of L_{OH}. In previous studies, aromatics accounted for the highest OFP and L_{OH} proportions in the PRD (Yu et al., 2020a; Tan et al., 2019). In Xi'an, the capital of Shaanxi Province, alkenes have been shown to have the highest proportion of L_{OH} and OFP (Song et al., 2020). The OFP of sampling sites around Lanzhou were mainly from aromatics, which accounted for 46.3% (Wu et al., 2019), due to the petrochemical industry there. Due to its abundant coal resources, Yulin has many coking plants. The exhaust gas from coking plants contains a lot of alkenes, the key species in O_3 formation, and aromatics (Zhang et al., 2020c).
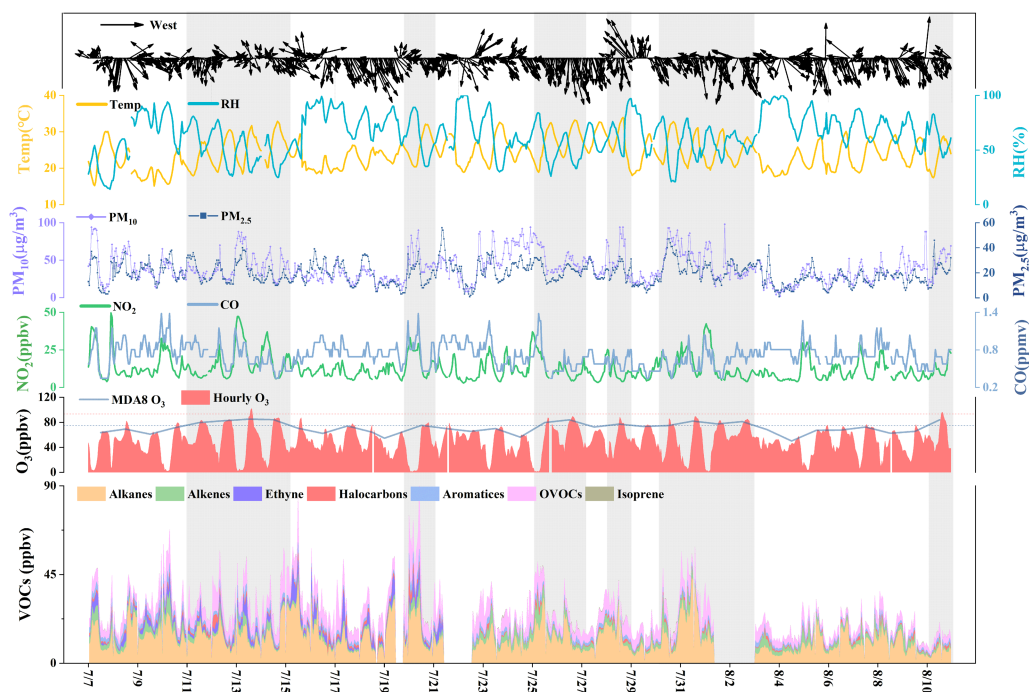
Figure 4 Time series of WS, WD, T, RH, O_3, $PM_{2.5}$, PM_{10}, NO_2, CO and VOCs at the EMB site during VOCs sampling period.
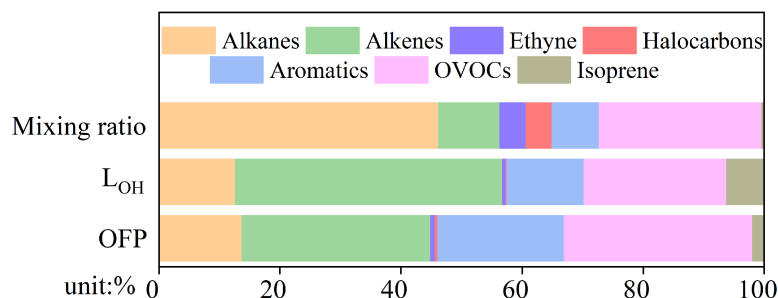
Figure 5 The ratio of concentrations, OH reaction (L_{OH}) and O_3 formation potential (OFP) of alkanes, alkenes, ethyne, halocarbons, aromatics, oxygenated VOCs (OVOCs) and isoprene.

DISCUSSION

The impact of meteorological parameters on O_3 concentration

Liu & Wang (2020) used the Community Multiscale Air Quality (CMAQ) modeling system and found that the impact of meteorological factors on O_3 trends varied by region and by year. Between 2013 and 2017, O_3 concentrations in China were affected by meteorological factors, which showed comparable or even greater effects than anthropogenic emissions. Meteorological conditions such as T, RH, WS, and WR directly affect surface O_3 concentrations via changes in chemical reaction rates, dilution, wet and dry removal,

Table 2 **Relationship between daily average temperature (T), relative humidity (RH) and wind speed (WS) and MDA8 and maximum daily 1-hour average O_3 concentrations (MDA1).**

	T	RH	WS
MDA8	0.547[**]	−0.286[**]	−0.088[**]
MDA1	0.519[**]	−0.250[**]	−0.164[**]

Notes.
[**] Correlation is significant at the 0.01 level.

and transport flux, or indirectly via changes in natural emissions (*Lu, Zhang & Shen, 2019b*; *Li et al., 2020c*). We focused on the relationship between meteorological parameters (T, RH, WS, and WR) and O_3 concentrations between May to August from 2017 to 2019 because O_3 pollution days mainly occurred during this period. The correlational analysis results are shown in Table 2. Table S5 shows the total number of days, number of MDA8 and MDA1 O_3 pollution days, and MDA8 and MDA1 O_3 exceedance probabilities in different ranges of T, RH, WS, and WR. The O_3 exceedance probability was calculated using the percentage of the number of O_3 pollution days across the total number of days. The influence of wind speed on ground O_3 concentrations was insignificant (−0.088). This result matches those in earlier studies (*Chen et al., 2020*; *Fan et al., 2020*).

T directly impacts chemical kinetic rates and the mechanistic pathway for O_3 formation (*Atkinson, 1990*). High RH days were always associated with more cloud cover, which can reduce photochemistry (*Kavassalis & Murphy, 2017*). The correlation coefficients between T and MDA8 O_3 and MDA1 O_3 were 0.547 and 0.519, respectively. Between RH and MDA8 O_3 and MDA1 O_3, the correlation coefficients were −0.286 and −0.250, respectively (Table 2). O_3 was positively correlated with T and negatively correlated with RH. Further statistical test results are shown in Table S5. The MDA8 (MDA1) O_3 exceedance probability of T in the ranges of 10−20 °C, 20−30 °C, and over 30 °C were 0.8% (0%), 27.7% (6.6%), and 81.82% (9.1%), respectively, and that of RH in the ranges of 20–40%, 40–60%, 60–80%, and 80–100% were 22.6% (6.1%), 31.3% (9.0%), 19.3% (2.3%), and 1.04% (0.0%), respectively. These results confirm that there is a correlation between O_3 and T and RH. When T was higher than 30 °C and RH was in the range of 40–60%, the probability of O_3 pollution events was higher.

The correlation coefficients between WS and MDA8 O_3 and MDA1 O_3 were −0.088 and −0.164, respectively, which indicated that the influence of WS on ground O_3 concentrations was insignificant. Table S5 shows that the MDA8 (MDA1) O_3 exceedance probability of WS in the range of 0–1.5 m/s, 1.5–3 m/s, 3–4.5 m/s, and greater than 4.5% were 22.5% (5.8%), 20.36% (3.3%), 9.26% (1.85%), and 0% (0%), respectively. As WS increased, the exceedance probability showed a downward trend. Generally, the increase in WS caused O_3 concentrations to decrease due to enhanced dry deposition, mixing, and dilution (*Dawson, Adams & Pandis, 2007*). Additionally, WS and WR affected O_3 concentrations by transporting O_3 and its precursors. The MDA8 (MDA1) O_3 exceedance probability of northerly, easterly, southerly, and westerly winds were 11.2% (5.1%), 28.0% (3.7%), 26.4% (5.7%), and 17.2% (5.7%), respectively. The effects of T, RH, and WS on MDA8 O_3 and MDA1 O_3 were similar. In contrast, the easterly winds showed the largest O_3 exceedance

probability of MDA8 O_3 and the southerly and westerly winds showed the greatest MDA1 O_3 exceedance probability. The results implied that T and RH can directly affect O_3 formation and loss. However, the influence of wind on O_3 concentrations was complex. In general, high T, low RH, and low WS were shown to cause O_3 pollution, especially when the T exceeded 25 °C, the RH was less than 60%, and the wind speed was less than 3 m/s. O_3 pollution days were predominantly observed when the wind was traveling from the east and south.

Regional transportation

Besides local formation, long-distance regional transportation also plays an important role in increasing O_3 concentration (*Hui et al., 2018*). Figures 6A–6C show the clustering analysis for May to August 2017 to 2019. In this study, when O_3 concentrations were greater than 75 ppbv, we identified this backward trajectory as a polluted trajectory. In 2017, a total of 487 backward trajectories were categorized into five clusters. Cluster a1 to a5 accounted for 49%, 21%, 3%, 13%. and 10% of the total trajectories, respectively. There was a total of 44 polluted trajectories in 2017. Cluster a1 to a5 contained 27, five, two, one, and eight polluted trajectories, respectively. Cluster a1' s air masses from Weinan in Shaanxi Province that crossed Yan'an to Yulin had the greatest impact on O_3 concentrations in Yulin in 2017. In 2018, there was a total of 492 backward trajectories across five clusters. Cluster b1 to b5 accounted for 13%, 23%, 27%, 31%, and 5% of the total trajectories, respectively. There was a total of 40 pollution trajectories in 2018. One, 10, 13, 12, and four pollution trajectories were grouped into clusters b1 to b5, respectively. Therefore, when the results of the cluster and the distribution of pollution trajectories were combined, the air masses of clusters b2, b3, and b4 had the greatest impact on the O_3 in Yulin in 2018. Cluster b2 was from Inner Mongolia. Cluster b3 came from Yan'an to Yulin. Cluster b4 came from Kaifeng in Henan Province, passing through Zhengzhou, Luoyang, Yuncheng in Shanxi Province, and Yan'an in Shaanxi Province. In 2019, a total of 492 backward trajectories were divided into three clusters. Cluster c1 to c3 accounted for 16%, 33%, and 51% of total trajectories, respectively. There was a total of 42 pollution trajectories in 2019. Thirty-two and 10 pollution trajectories were grouped into cluster c2 and c3, respectively. Therefore, the air masses of cluster c2, which came from Linfen in Shanxi and passed through Weinan and Yan'an in Shaanxi Province to Yulin, had the greatest impact on the O_3 in Yulin in 2019. Fenwei Plain is to the southeast of Yulin and has 11 cities including Weinan, Luoyang, and Yuncheng, mentioned above. Fenwei Plain has a high O_3 concentration because it has more industry and a larger population (*Lu et al., 2019a*; *Wang et al., 2020a*). The airflows from Yan'an and FenWei Plain between May and August may aggravate O_3 pollution in Yulin.

Sensitivity analysis

The relationships between O_3 and VOCs and NO_x are nonlinear. In order to establish effective O_3 control measures, these relationships must be explored. In this study, we applied two methods to evaluate O_3-VOC-NO_x sensitivity in Yulin: the RIR, which was mentioned in sec2.3, and the EKMA (*Carter, Winer & PittsJr, 1982*). The average hourly
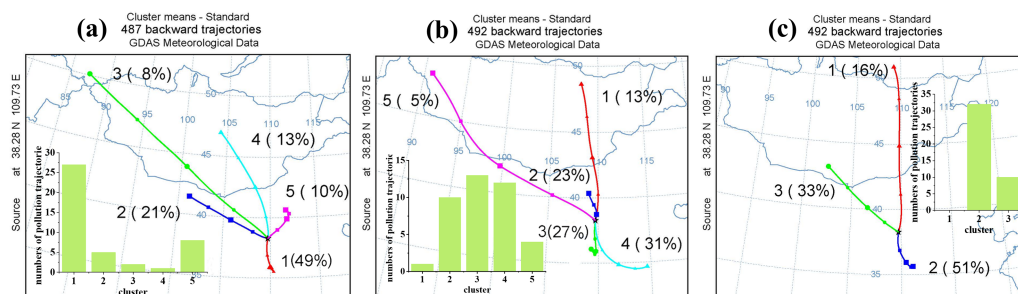
Figure 6 Result of cluster analysis of backward trajectories in Yulin from May to August 2017 (A), 2018 (B), 2019 (C). And the number of polluted trajectories in every cluster. The backward trajectory with O_3 concentrations over 75 ppbv is identified as a polluted trajectory.
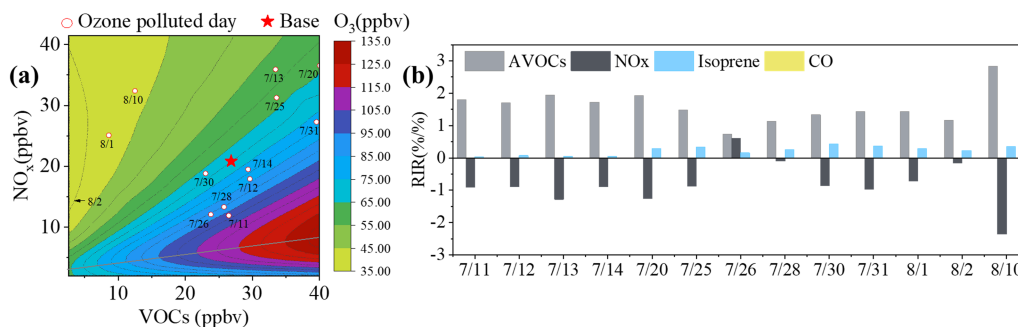
Full-size DOI: 10.7717/peerj.11322/fig-6

Figure 7 EKMA and Relative incremental reactivity (RIR). (A) Contour plot of MDA8 as a function of VOC reactivity and NOx concentrations (EKMA), the star represents the base scenario and circles represent O_3 pollution days (A). (B) Relative incremental reactivity (RIR) for AVOCs, isoprene, CO and NO_x on O_3 pollution days.

Full-size DOI: 10.7717/peerj.11322/fig-7

VOC concentrations during the sampling period were put in the OBM model as a base scenario. By increasing or decreasing the ratio of precursors, we were able to simulate the changes in MDA8 O_3. The relationship between MDA8 O_3 and the relative changes of anthropogenic VOCs (AVOCs) and NO_x can be expressed using a contour plot for MDA8 O_3, which we named EKMA (Fig. 7A). Isoprene was mainly emitted by the biogenic source and was difficult to control. Therefore, the AVOCs excluded isoprene. The EKMA plot was split into two parts by a ridgeline that denoted the local maxima of the rate of O_3 formation (*Li et al., 2020b*; *Hui et al., 2018*). The upper-left and lower-right areas represent the O_3 formation under VOC-limited and NO_x-limited conditions, respectively. In Fig. 7A, the circles and pentagram represent pollution days and the base scenario, respectively. These points were all located in the VOC-limited regime and showed the negative effects of NO_x reduction in response to O_3 production control. Previous studies reported that in China, unban areas, rural regions, and urban agglomerations were under VOC-limited, NO_x-limited, and VOC-NO_x-limited conditions (*Liu et al., 2019*; *Wang et al., 2017a*), respectively.

Figure 7B shows the RIR values for AVOCs, isoprene, CO, and NO$_x$ during pollution days. The RIR values for AVOCs were in the range of 0.73–2.83%/%, which was significantly higher than those for isoprene (0.22–0.42%/%) and CO (under 0.01%/%). This suggested that AVOCs played a more significant role in O$_3$ formation during these EPs, while the influence of isoprene, especially CO, was negligible. Excluding 26 July, the RIR values for NO$_x$ were between −0.26 and −0.10%/%, indicating that the O$_3$ formation during these days was in the VOC-limited regime. This result was consistent with that of EKMA. However, on 26 July, the RIR values of NO$_x$ and VOCs were 0.60 and 0.73, respectively, and these two positive values with a small difference implied that the O$_3$ formation on 26 July was controlled by both VOCs and NO$_x$. This result was contrary to that of the EKMA plot, which may be because the EKMA simulation was based on the average of the sampling period. The average RIR values for AVOCs from EP1 to EP6 were 1.79%/%, 1.92%/%, 1.11%/%, 1.13%/%, 1.34%/%, and 2.83%/%, respectively, and for NO$_x$ were -0.99%/%, 1.26%/%, -0.14%/%, -0.10%/%, -0.68%/%, and -2.36%/%, respectively. This demonstrated that these EPs were all in the VOC-limited regime. The absolute RIR values of the AVOCs were larger than those of the NO$_x$, suggesting that O$_3$ formation was most sensitive to AVOC reduction.

O$_3$ control strategies

It is necessary to discuss how much AVOCs should be controlled for the most efficient O$_3$ reduction. Using the sampling period as an example, we will discuss O$_3$ control measures. Figure 8A shows the increments of the MDA8 O$_3$ response (positive and negative values represented the increase and decrease in O$_3$ compared to the base case with no VOC or NO$_x$ reductions, respectively) to different emission reductions in AVOCs and NO$_x$ (AVOC reduction/NO$_x$ reduction=1:2, 1:1, 2:1, 3:1, or 4:1, and only reducing AVOCs or NO$_x$). The horizontal axis represents the combined reduction percentage of AVOCs and NO$_x$. For instance, a total reduction percentage of 120% indicates that there were both 60% reductions in AVOCs and NO$_x$ emissions for AVOC/NO$_x$=1:1, or 80% and 40% reductions in the AVOC and NO$_x$ emissions, respectively, for AVOC/NO$_x$=2:1. When the AVOC/NO$_x$ ratio was more than 1:1, namely if the AVOC emission was reduced more than NO$_x$, the O$_3$ concentration would decline. When a certain O$_3$ reduction target was achieved, the VOC and NO$_x$ ratio was higher and the total emission reduction was lower. For example, to reduce O$_3$ concentration by 5%, the total reduction emissions of AVOC and NO$_x$ were 12%, 20%, and 174% for an abatement AVOC/NO$_x$ ratio of 4:1, 2:1, and 1:1, respectively, or by only cutting AVOC emissions by 7%. Only cutting AVOC emissions seemed to be the most efficient way to control O$_3$. However, NO$_2$ is one of the most significant ambient air pollutants that can influence ambient air quality. NO$_x$ needs to be reduced since it is an important precursor of PM$_{2.5}$. It is important to cooperatively control the emission of AVOCs and NO$_x$. During sampling periods, the mean and highest MDA8 O$_3$ concentrations were 79 and 102 ppbv, respectively, which exceeded the Nation Grade by 5% and 36%. According to this, we set four O$_3$ control targets, 5%, 10%, 30%, and 40%, to explore the abatement percentages of AVOCs and NO$_x$ (Fig. 8B). To achieve the O$_3$ control target of 5%, AVOC emissions needed to be reduced 10%–90%, with NO$_x$ also in
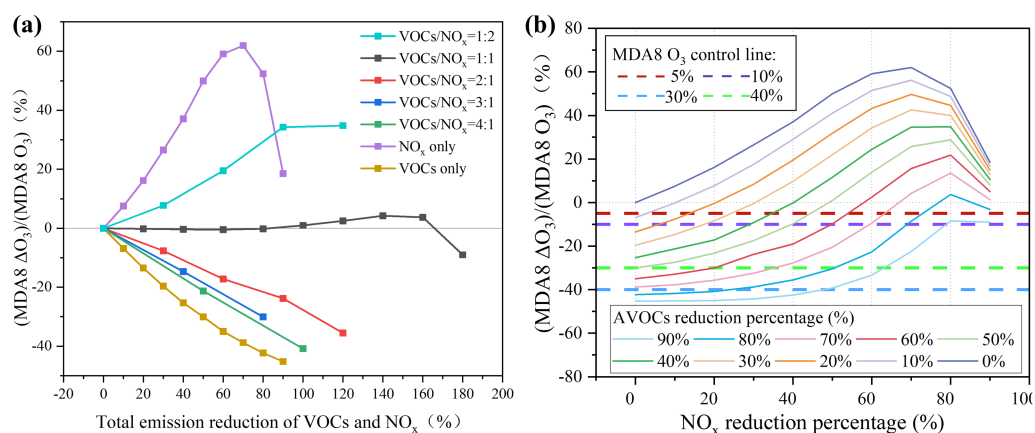
Figure 8 (A) The increment percentage of MDA8 O$_3$ are shown under different NO$_x$ and VOCs reduction pathways and (B) the reduction percentages of NO$_x$ and VOCs.

Full-size ☒ DOI: 10.7717/peerj.11322/fig-8

the range of 10%–90%. To achieve the O$_3$ control target of 10%, AVOC emissions needed to be reduced 20% to 90% with NO$_x$ in the range of 5% to 80%. However, to achieve the targets of 30% and 40%, the AVOC emissions needed to be reduced by at least 60% and 80%, respectively. Even though more stringent VOC and NO$_x$ control measures have been implemented, it is still challenging to achieve the 30% and 40% O$_3$ control objectives. Q$_{true}$/Q$_{expected}$ was an appropriate index to decide how many factors were optimal in the PMF model. Here, we evaluated four to 10 factor solutions and found that the Qtrue/Qexpected values of different resolved numbers and that eight to nine factors were the lowest (Fig. S2). Therefore, we identified eight types of major pollution sources using PMF source analysis (Fig. 9 and Fig. S3). Factor 1 had a high percentage of aromatics and a relatively high ratio of toluene. In previous studies, toluene was the most abundant VOC species in painting and factor 1 was considered to be the source of the solvent (*Wang et al., 2014*). Coking plants and the petrochemical industry are pillars in Yulin and emit a lot of ethene (*Zhang et al., 2020c*; *Han et al., 2018*), so we considered factor 2 to be industrial sources. The main source of isoprene in the city is plant emissions (*Zhang et al., 2020a*; *Loivamaki et al., 2007*) and factor 3 is considered a biological source. Factor 4 was characterized by a high percentage of ethane and high loadings of OVOCs. Previous studies in Shenzhen and Wangdu found that background pollution largely contributed to OVOCs (*Han et al., 2019*). Factor 4 was considered background pollution. High percentages of propane, acetylene, n-butane, cyclohexane, ethylbenzene, o-xylene, isobutane, m/p-xylene, and n-hexane are found in vehicle exhaust (*Fan et al., 2020*), and these characteristics are consistent with factors 5 and 7. The proportion of isopentane in gasoline exhaust is more than that found in diesel exhaust (*Ly et al., 2020*). The proportion of aromatic hydrocarbons is higher in gasoline vehicles than in diesel vehicles because aromatic hydrocarbons are the main contributor to octane in gasoline, and gasoline is more volatile than diesel (*Huang et al., 2020*). Factors 5 and 7 were considered gasoline exhaust and diesel exhaust, respectively. Isopentane is mainly distributed in factor 6 and is a typical marker of fuel evaporation
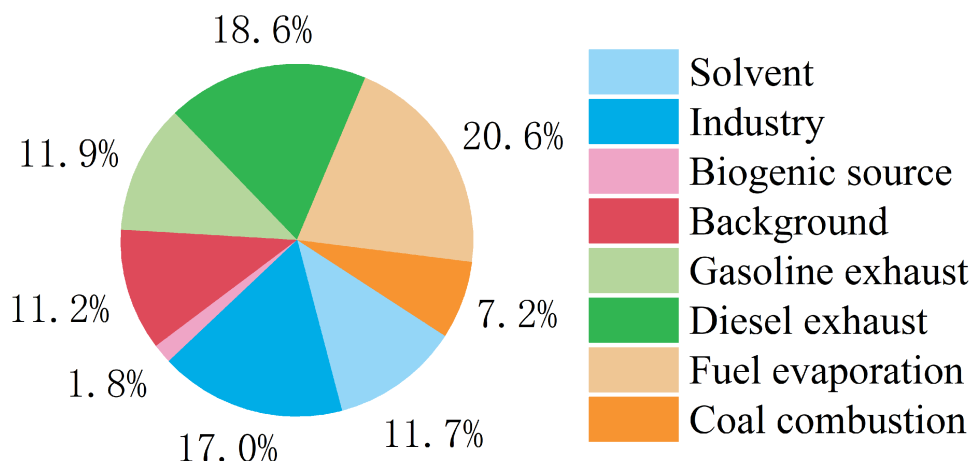
Figure 9 Relative contributions of different sources to VOCs during study period.

Full-size 🖼 DOI: 10.7717/peerj.11322/fig-9

(*Liu et al., 2008*), so factor 6 was considered fuel evaporation. Factor 8 was characterized by a high percentage of ethane, ethene, and 1-butene. Previous studies reported that VOCs emitted from coal combustion (*Zhang et al., 2020a*) are mainly C2-C3 alkenes and C2-C3 alkanes. Factor 7 was considered coal combustion. Vehicle emissions count for 51.1% of emissions (Fig. 9) and diesel exhaust is most dominant. Industrial sources account for 17.0%. Previous emission reduction strategies focused on reducing vehicle and industry emissions, especially diesel exhaust.

CONCLUSION

We measured ambient O_3 levels at four National Environmental Monitoring Stations. The MDA8 90th O_3 concentrations in Yulin were 72, 72, and 75 ppbv from 2017 to 2019, respectively, and they showed an increasing trend. The EMB site had the highest O_3 levels. Because the HPGP site is a traffic-intensive area, this site had more NO emissions from trucks during night transportation that led to lower night concentrations than at the other sites. O_3 concentrations were higher in summer and lower in winter, reflecting an obvious seasonal cycle, and the pollution days occurred between May and August.

Our O_3 and T, RH, and WS correlation analysis results implied that O_3 had a positive correlation with T and a negative correlation with RH. Through statistical analysis, we found that when T was greater than 25 °C, RH was lower than 60%, WS was less than 3m/s, and the WD was northerly, the probability of MDA8 O_3 exceeding the Grade II Standard increased. Using the HYSPLIT model to calculate the backward trajectories from May to August 2017 to 2019, we saw that the O_3 concentration in summer was greatly affected by transportation on the Fenwei Plain.

The VOC sampling period from July 7th to August 10th had 13 O_3 pollution days across six EPs. During this period, the average O_3 and TVOCs were 50 ± 22 ppbv and 26 ± 12 ppbv, respectively. Alkane was the most abundant VOC group. As a result of the OFP and OH reaction, alkenes were the most important VOC species for O_3 formation. Using the

OBM-calculated EKMA plot and RIR value indicated that Yulin is located in a VOC-limited regime. This suggested that a slight decrease of NO_x may increase O_3 concentration. The AVOC RIR value was the highest and was the key VOC that needed to be primarily controlled. In regard to O_3 control strategies, when the reduction of AVOC/NO_x is higher than 1:1, the O_3 will decrease. According to the average and maximum MDA8 O_3, we set four targets for decreased O_3 emissions. For O_3 concentrations to decrease by 5%, AVOCs and NO_x are needed to reduce emissions by 10%–90%. For O_3 concentrations to decrease by 10%, AVOCs and NO_x are needed to reduce emissions by 20%–90% and 5%–80%, respectively. However, the 30% and 40% targets will be difficult to achieve. The PMF model showed that vehicle exhaust and coal chemical industry emissions are the main sources of AVOC emission reductions.

ACKNOWLEDGEMENTS

ADDITIONAL INFORMATION AND DECLARATIONS

Funding

Grant Disclosures

Competing Interests

The authors declare there are no competing interests.

Author Contributions

- Manfei Yin and Xin Zhang performed the experiments, analyzed the data, prepared figures and/or tables, and approved the final draft.
- Yunfeng Li performed the experiments, prepared figures and/or tables, and approved the final draft.

- Kai Fan analyzed the data, prepared figures and/or tables, and approved the final draft.
- Hong Li performed the experiments, authored or reviewed drafts of the paper, and approved the final draft.
- Rui Gao and Jinjuan Li conceived and designed the experiments, authored or reviewed drafts of the paper, and approved the final draft.

Data Availability

The following information was supplied regarding data availability:

The raw measurements are available in the Supplemental Files.

Supplemental Information

Supplemental information for this article can be found online at http://dx.doi.org/10.7717/peerj.11322#supplemental-information.

REFERENCES

Atkinson R. 1990. Gas-phase tropospheric chemistry of organic compounds: a review. *Atmospheric Environment Part A General Topics* **24**:1–41 DOI 10.1016/0960-1686(90)90438-S.

Atkinson R, Arey J. 2004. Atmospheric degradation of volatile organic compounds. *Chemical Reviews* **103**:4605–4638 DOI 10.1021/cr0206420.

Cao JJ, Chow JC, Watson JG, Wu F, Han YM, Jin ZD, Shen ZX, An ZS. 2008a. Size-differentiated source profiles for fugitive dust in the Chinese Loess Plateau. *Atmospheric Environment* **42**:2261–2275 DOI 10.1016/j.atmosenv.2007.12.041.

Cao JJ, Shen ZX, Chow JC, Watson JG, Lee SC, Tie XX, Ho KF, Wang GH, Han YM. 2012. Winter and summer PM2.5 chemical compositions in fourteen chinese cities. *Journal of the Air & Waste Management Association* **62**:1214–1226 DOI 10.1080/10962247.2012.701193.

Cao JJ, Zhu CS, Chow JC, Liu WG, Han YM, Watson JG. 2008b. Stable carbon and oxygen isotopic composition of carbonate in fugitive dust in the Chinese Loess Plateau. *Atmospheric Environment* **42**:9118–9122 DOI 10.1016/j.atmosenv.2008.09.043.

Cardelino CA, Chameides WL. 1995. An observation-based model for analyzing ozone precursor relationships in the urban atmosphere. *Journal of the Air & Waste Management Association* **45**:161–180 DOI 10.1080/10473289.1995.10467356.

Carter WPL. 2009. *Updated maximum incremental reactivity scale and hydrocarbon bin reactivities for regulatory applications.* College of Engineering Center for Environmental Research and Technology University of California. *Available at https://ww3.arb.ca.gov/regact/2009/mir2009/mir10.pdf* .

Carter WP, Winer AM, Pitts Jr JN. 1982. Effects of kinetic mechanisms and hydrocarbon composition on oxidant-precursor relationships predicted by the EKMA isopleth technique. *Atmospheric Environment* **16**:113–120 DOI 10.1016/0004-6981(82)90318-3.

Chen Z, Li R, Chen D, Zhuang Y, Gao B, Yang L, Li M. 2020. Understanding the causal influence of major meteorological factors on ground ozone concentrations across China. *Journal of Cleaner Production* **242**:118498 DOI 10.1016/j.jclepro.2019.118498.

Chen X, Situ S, Zhang Q, Wang X, Sha C, Zhouc L, Wu L, Wu L, Ye L, Li C. 2019. The synergetic control of NO2 and O3 concentrations in a manufacturing city of southern China. *Atmospheric Environment* **201**:402–416 DOI 10.1016/j.atmosenv.2018.12.021.

Cohen MD, Stunder BJB, Rolph GD, Draxler RR, Stein AF, Ngan F. 2015. NOAA's HYSPLIT atmospheric transport and dispersion modeling system. *Bulletin of the American Meteorological Society* **96**:2059–2077 DOI 10.1175/bams-d-14-00110.1.

Crutzen PJ. 2016. Photochemical reactions initiated by and influencing ozone in unpolluted tropospheric air. *Tellus* **26**:47–57 DOI 10.3402/tellusa.v26i1-2.9736.

David LM, Nair PR. 2011. Diurnal and seasonal variability of surface ozone and NOxat a tropical coastal site: association with mesoscale and synoptic meteorological conditions. *Journal of Geophysical Research* **116**:D10303 DOI 10.1029/2010jd015076.

Dawson JP, Adams PJ, Pandis SN. 2007. Sensitivity of ozone to summertime climate in the eastern USA: a modeling case study. *Atmospheric Environment* **41**:1494–1511 DOI 10.1016/j.atmosenv.2006.10.033.

Draxler RR, Hess GD. 1998. An overview of the HYSPLIT_4 modeling system for trajectories, dispersion, and deposition. *Australian Meteorological Magazine* **47**:295–308.

Duan J, Tan J, Yang L, Wu S, Hao J. 2008. Concentration, sources and ozone formation potential of volatile organic compounds (VOCs) during ozone episode in Beijing. *Atmospheric Research* **88**:25–35 DOI 10.1016/j.atmosres.2007.09.004.

Fan M-Y, Zhang Y-L, Lin Y-C, Li L, Xie F, Hu J, Mozaffar A, Cao F. 2020. Source apportionments of atmospheric volatile organic compounds in Nanjing, China during high ozone pollution season. *Chemosphere* **263**:128025 DOI 10.1016/j.chemosphere.2020.128025.

Fang X, Xiao H, Sun H, Liu C, Zhang Z, Xie Y, Liang Y, Wang F. 2020. Characteristics of Ground-Level Ozone from 2015 to 2018 in BTH Area, China. *Atmosphere* **11**:130 DOI 10.3390/atmos11020130.

Han D, Gao S, Fu Q, Cheng J, Chen X, Xu H, Liang S, Zhou Y, Ma Y. 2018. Do volatile organic compounds (VOCs) emitted from petrochemical industries affect regional PM2.5? *Atmospheric Research* **209**:123–130 DOI 10.1016/j.atmosres.2018.04.002.

Han Y, Huang X, Wang C, Zhu B, He L. 2019. Characterizing oxygenated volatile organic compounds and their sources in rural atmospheres in China. *Journal of the Electrochemical Society* **81**:148–155 DOI 10.1016/j.jes.2019.01.017.

Hao X, Song M, Feng Y, Zhang W. 2019. De-capacity policy effect on China's coal industry. *Energies* **12**:2331 DOI 10.3390/en12122331.

He Z, Wang X, Ling Z, Zhao J, Wang Z. 2019. Contributions of different anthropogenic volatile organic compound sources to ozone formation at a receptor site in the Pearl River Delta region and its policy implications. *Atmospheric Chemistry Physics* **19**:8801–8816 DOI 10.5194/acp-19-8801-2019.

He Z, Zhang X, Li Y, Zhong X, Li H, Gao R, Li J. 2020. Characterizing carbonyl compounds and their sources in Fuzhou ambient air, southeast of China. *Peerj* **8**:e10227 DOI 10.7717/peerj.10227.

Hou X, Zhuang G, Sun Y, An Z. 2006. Characteristics and sources of polycyclic aromatic hydrocarbons and fatty acids in PM2.5 aerosols in dust season in China. *Atmospheric Environment* **40**:3251–3262 DOI 10.1016/j.atmosenv.2006.02.003.

Hu XM, Ma Z, Lin W, Zhang H, Hu J, Wang Y, Xu X, Fuentes JD, Xue M. 2014. Impact of the Loess Plateau on the atmospheric boundary layer structure and air quality in the North China Plain: a case study. *Science of The Total Environment* **499**:228–237 DOI 10.1016/j.scitotenv.2014.08.053.

Huang H, Hu H, Zhang J, Liu X. 2020. Characteristics of volatile organic compounds from vehicle emissions through on–road test in Wuhan, China. *Environmental Research* **188**:109802 DOI 10.1016/j.envres.2020.109802.

Hui L, Liu X, Tan Q, Feng M, An J, Qu Y, Zhang Y, Deng Y, Zhai R, Wang Z. 2020. VOC characteristics, chemical reactivity and sources in urban Wuhan, central China. *Atmospheric Environment* **224**:117340 DOI 10.1016/j.atmosenv.2020.117340.

Hui L, Liu X, Tan Q, Feng M, An J, Qu Y, Zhang Y, Jiang M. 2018. Characteristics, source apportionment and contribution of VOCs to ozone formation in Wuhan, Central China. *Atmospheric Environment* **192**:55–71 DOI 10.1016/j.atmosenv.2018.08.042.

Hui L, Ma T, Gao Z, Gao J, Wang Z, Xue L, Liu H, Liu J. 2021. Characteristics and sources of volatile organic compounds during high ozone episodes: a case study at a site in the eastern Guanzhong Plain, China. *Chemosphere* **265**:129072 DOI 10.1016/j.chemosphere.2020.129072.

Kavassalis SC, Murphy JG. 2017. Understanding ozone-meteorology correlations: a role for dry deposition. *Geophysical Research Letters* **44**:2922–2931 DOI 10.1002/2016gl071791.

Lei Y, Shen Z, Wang Q, Zhang T, Cao J, Sun J, Zhang Q, Wang L, Xu H, Tian JJAr. 2018. Optical characteristics and source apportionment of brown carbon in winter PM_(2.5) over Yulin in Northern China. *Atmospheric Research* **213**:27–33 DOI 10.1016/j.atmosres.2018.05.018.

Li L, An J, Huang L, Yan R, Huang C, Yarwood G. 2019. Ozone source apportionment over the Yangtze River Delta region, China: investigation of regional transport, sectoral contributions and seasonal differences. *Atmospheric Environment* **202**:269–280 DOI 10.1016/j.atmosenv.2019.01.028.

Li K, Jacob DJ, Shen L, Lu X, De Smedt I, Liao H. 2020c. Increases in surface ozone pollution in China from 2013 to 2019: anthropogenic and meteorological influences. *Atmospheric Chemistry and Physics* **20**:11423–11433 DOI 10.5194/acp-20-11423-2020.

Li J, Wang Z, Chen L, Lian L, Li Y, Zhao L, Zhou S, Mao X, Huang T, Gao H, Ma J. 2020b. WRF-Chem simulations of ozone pollution and control strategy in petrochemical industrialized and heavily polluted Lanzhou City, Northwestern China. *Science of The Total Environment* **737**:139835 DOI 10.1016/j.scitotenv.2020.139835.

Li J, Zhao Y, Han L, Zhang G, Liu R. 2017. Moisture variation inferred from a nebkha profile correlates with vegetation changes in the southwestern Mu Us Desert of China over one century. *Science of The Total Environment* **598**:797–804 DOI 10.1016/j.scitotenv.2017.03.145.

Li B, Zhou Z, Xue Z, Wei P, Ren Y, Cao L, Feng X, Yao Q, Ma J, Xu P, Chen X. 2020a. Study on the pollution characteristics and sources of ozone in typical Loess Plateau City. *Atmosphere* **11**:555 DOI 10.3390/atmos11060555.

Liu N, Lin W, Ma J, Xu W, Xu X. 2019. Seasonal variation in surface ozone and its regional characteristics at global atmosphere watch stations in China. *Journal of Environmental Sciences* **77**:291–302 DOI 10.1016/j.jes.2018.08.009.

Liu Y, Shao M, Fu L, Lu S, Zeng L, Tang D. 2008. Source profiles of volatile organic compounds (VOCs) measured in China: Part I. *Atmospheric Environment* **42**:6247–6260 DOI 10.1016/j.atmosenv.2008.01.070.

Liu LY, Shi PJ, Gao SY, Zou XY, Erdon H, Yan P, Li XY, Ta WQ, Wang JH, Zhang CL. 2004. Dustfall in China's western loess plateau as influenced by dust storm and haze events. *Atmospheric Environment* **38**:1699–1703 DOI 10.1016/j.atmosenv.2004.01.003.

Liu Y, Wang T. 2020. Worsening urban ozone pollution in China from 2013 to 2017 – Part 1: The complex and varying roles of meteorology. *Atmospheric Chemistry and Physics* **20**:6305–6321 DOI 10.5194/acp-20-6305-2020.

Loivamaki M, Gilmer F, Fischbach RJ, Sorgel C, Bachl A, Walter A, Schnitzler JP. 2007. Arabidopsis, a model to study biological functions of isoprene emission? *Plant Physiology* **144**:1066–1078 DOI 10.1104/pp.107.098509.

Lu X, Zhang L, Chen Y, Zhou M, Zheng B, Li K, Liu Y, Lin J, Fu T-M, Zhang Q. 2019a. Exploring 2016–2017 surface ozone pollution over China: source contributions and meteorological influences. *Atmospheric Chemistry and Physics* **19**:8339–8361 DOI 10.5194/acp-19-8339-2019.

Lu X, Zhang L, Shen L. 2019b. Meteorology and climate influences on tropospheric ozone: a review of natural sources, chemistry, and transport patterns. *Current Pollution Reports* **5**:238–260 DOI 10.1007/s40726-019-00118-3.

Ly BT, Kajii Y, Nguyen TY, Shoji K, Van DA, Do TN, Nghiem TD, Sakamoto Y. 2020. Characteristics of roadside volatile organic compounds in an urban area dominated by gasoline vehicles, a case study in Hanoi. *Chemosphere* **254**:126749 DOI 10.1016/j.chemosphere.2020.126749.

Lyu X, Wang N, Guo H, Xue L, Jiang F, Zeren Y, Cheng H, Cai Z, Han L, Zhou Y. 2019. Causes of a continuous summertime O_3 pollution event in Jinan, a central city in the North China Plain. *Atmospheric Chemistry and Physics* **19**:3025–3042 DOI 10.5194/acp-19-3025-2019.

Paatero P, Tapper U. 1994. Positive matrix factorization: a non-negative factor model with optimal utilization of error estimates of data values. *Environmetrics* **5**:111–126 DOI 10.1002/env.3170050203.

Song M, Li X, Yang S, Yu X, Zhou S, Yang Y, Chen S, Dong H, Liao K, Chen Q, Lu K, Zhang N, Cao J, Zeng L, Zhang Y. 2020. Spatiotemporal variation, sources, and secondary transformation potential of VOCs in Xi'an, China. *Atmospheric Chemistry Physics* **21**:4939–4958 DOI 10.5194/acp-2020-704.

Sun X, Wang H, Guo Z, Lu P, Song F, Liu L, Liu J, Rose NL, Wang F. 2020. Positive matrix factorization on source apportionment for typical pollutants in different environmental media: a review. *Environmental Science: Processes & Impacts* **22**:239–255 DOI 10.1039/c9em00529c.

Tan Z, Lu K, Jiang M, Su R, Dong H, Zeng L, Xie S, Tan Q, Zhang Y. 2018. Exploring ozone pollution in Chengdu, southwestern China: a case study from radical chemistry to O3-VOC-NOx sensitivity. *Science of The Total Environment* **636**:775–786 DOI 10.1016/j.scitotenv.2018.04.286.

Tan Z, Lu K, Jiang M, Su R, Zhang Y. 2019. Daytime atmospheric oxidation capacity in four Chinese megacities during the photochemically polluted season: a case study based on box model simulation. *Atmospheric Chemistry Physics* **19**:3493–3513 DOI 10.5194/acp-19-3493-2019.

Wang M, Chen W, Zhang L, Qin W, Zhang Y, Zhang X, Xie X. 2020b. Ozone pollution characteristics and sensitivity analysis using an observation-based model in Nanjing, Yangtze River Delta Region of China. *Journal of Environmental Sciences* **93**:13–22 DOI 10.1016/j.jes.2020.02.027.

Wang WN, Cheng TH, Gu XF, Chen H, Guo H, Wang Y, Bao FW, Shi SY, Xu BR, Zuo X, Meng C, Zhang XC. 2017b. Assessing spatial and temporal patterns of observed ground-level ozone in China. *Scientific Reports* **7**:3651 DOI 10.1038/s41598-017-03929-w.

Wang H, Qiao Y, Chen C, Lu J, Dai H, Qiao L, Lou S, Huang C, Li L, Jing S, Wu J. 2014. Source profiles and chemical reactivity of volatile organic compounds from solvent use in Shanghai, China. *Aerosol and Air Quality Research* **14**:301–310 DOI 10.4209/aaqr.2013.03.0064.

Wang F, Qiu X, Cao J, Peng L, Zhang N, Yan Y, Li R. 2020a. Policy-driven changes in the health risk of PM2.5 and O3 exposure in China during 2013–2018. *Science of The Total Environment* **757**:143775 DOI 10.1016/j.scitotenv.2020.143775.

Wang X, Shen Z, Cao J, Zhang L, Liu L, Li J, Liu S, Sun Y. 2012. Characteristics of surface ozone at an urban site of Xi'an in Northwest China. *Journal of Environmental Monitoring* **14**:116–126 DOI 10.1039/c1em10541h.

Wang T, Xue L, Brimblecombe P, Lam YF, Li L, Zhang L. 2017a. Ozone pollution in China: a review of concentrations, meteorological influences, chemical precursors, and effects. *Science of The Total Environment* **575**:1582–1596 DOI 10.1016/j.scitotenv.2016.10.081.

Wang Q, Zhuang G, Li J, Huang K, Zhang R, Jiang Y, Lin Y, Fu JS. 2011. Mixing of dust with pollution on the transport path of Asian dust–revealed from the aerosol over Yulin, the north edge of Loess Plateau. *Science of The Total Environment* **409**:573–581 DOI 10.1016/j.scitotenv.2010.10.032.

Wu Y, Hu J, Wang H, Li H, Zhang H, Chai F, Wang S. 2019. The Characteristics of Ambient Non-Methane Hydrocarbons (NMHCs) in Lanzhou, China. *Atmosphere* **10**:745 DOI 10.3390/atmos10120745.

Xiaoye Z. 2002. Characterization of atmospheric aerosol over xian in the south margin of the Loess Plateau, China. *Atmospheric Environment* **36**:4189–4199 DOI 10.1016/S1352-2310(02)00347-3.

Xu J, Ma JZ, Zhang XL, Xu XB, Xu XF, Lin WL, Wang Y, Meng W, Ma ZQ. 2011. Measurements of ozone and its precursors in Beijing during summertime: impact of urban plumes on ozone pollution in downwind rural areas. *Atmospheric Chemistry and Physics* **11**:12241–12252 DOI 10.5194/acp-11-12241-2011.

Yan S, Cao H, Chen Y, Wu C, Hong T, Fan H. 2016b. Spatial and temporal characteristics of air quality and air pollutants in 2013 in Beijing. *Environmental Science and Pollution Research International* **23**:13996–14007 DOI 10.1007/s11356-016-6518-3.

Yan C, Nie W, Äijälä M, Rissanen MP, Canagaratna MR, Massoli P, Junninen H, Jokinen T, Sarnela N, Häme S, Schobesberger S, Canonaco F, Prevot ASH, Petäjä T, Kulmala M, Sipilä M, Worsnop DR, Ehn M. 2016a. Source characterization of highly oxidized multifunctional compounds in a boreal forest environment using positive matrix factorization. *Atmospheric Chemistry and Physics* **16**:1680–7316 DOI 10.5194/acp-16-12715-2016.

Yu D, Tan Z, Lu K, Ma X, Li X, Chen S, Zhu B, Lin L, Li Y, Qiu P, Yang X, Liu Y, Wang H, He L, Huang X, Zhang Y. 2020a. An explicit study of local ozone budget and NOx-VOCs sensitivity in Shenzhen China. *Atmospheric Environment* **224**:117304 DOI 10.1016/j.atmosenv.2020.117304.

Yu S, Yin S, Zhang R, Wang L, Su F, Zhang Y, Yang J. 2020b. Spatiotemporal characterization and regional contributions of O3 and NO2: an investigation of two years of monitoring data in Henan, China. *Journal of Environmental Sciences* **90**:29–40 DOI 10.1016/j.jes.2019.10.012.

Zeng Y, Cao Y, Qiao X, Seyler BC, Tang Y. 2019. Air pollution reduction in China: recent success but great challenge for the future. *Science of The Total Environment* **663**:329–337 DOI 10.1016/j.scitotenv.2019.01.262.

Zhai X, Cheng Z, Chang S, Ai X, Zhang X. 2020. An analysis on the current situation of energy development and its environmental problems in Yulin City. *Energy Reports* **6**:15–20 DOI 10.1016/j.egyr.2019.08.011.

Zhang K, Li L, Huang L, Wang Y, Huo J, Duan Y, Wang Y, Fu Q. 2020b. The impact of volatile organic compounds on ozone formation in the suburban area of Shanghai. *Atmospheric Environment* **232**:117511 DOI 10.1016/j.atmosenv.2020.117511.

Zhang F, Shang X, Chen H, Xie G, Fu Y, Wu D, Sun W, Liu P, Zhang C, Mu Y, Zeng L, Wan M, Wang Y, Xiao H, Wang G, Chen J. 2020a. Significant impact of coal combustion on VOCs emissions in winter in a North China rural site. *Science of The Total Environment* **720**:137617 DOI 10.1016/j.scitotenv.2020.137617.

Zhang Q, Shen Z, Cao J, Ho K, Zhang R, Bie Z, Chang H, Liu S. 2014a. Chemical profiles of urban fugitive dust over Xi'an in the south margin of the Loess Plateau, China. *Atmospheric Pollution Research* **5**:421–430 DOI 10.5094/apr.2014.049.

Zhang X, Wang D, Liu Y, Cui Y, Xue Z, Gao Z, Du J. 2020c. Characteristics and ozone formation potential of volatile organic compounds in emissions from

a typical Chinese coking plant. *Journal of Environmental Sciences* **95**:183–189
DOI 10.1016/j.jes.2020.03.018.

Zhang Q, Yuan B, Shao M, Wang X, Lu S, Lu K, Wang M, Chen L, Chang CC, Liu SC. 2014b. Variations of ground-level O3 and its precursors in Beijing in summer-time between 2005 and 2011. *Atmospheric Chemistry and Physics* **14**:6089–6101 DOI 10.5194/acp-14-6089-2014.

Zhang Q, Zheng Y, Tong D, Shao M, Wang S, Zhang Y, Xu X, Wang J, He H, Liu W, Ding Y, Lei Y, Li J, Wang Z, Zhang X, Wang Y, Cheng J, Liu Y, Shi Q, Yan L, Geng G, Hong C, Li M, Liu F, Zheng B, Cao J, Ding A, Gao J, Fu Q, Huo J, Liu B, Liu Z, Yang F, He K, Hao J. 2019. Drivers of improved PM2.5 air quality in China from 2013 to 2017. *Proceedings of the National Academy of Sciences of the United States of America* **116**:24463–24469 DOI 10.1073/pnas.1907956116.

Zheng D, Wang Y, Shao Y, Wang L. 2019. The vegetation dynamics and climate change responses by leaf area index in the Mu Us Desert. *Sustainability* **11**:3151 DOI 10.3390/su11113151.

Zhu Y, Yan X, Kong X, Tong Q, Li Y, Huang G, Li Y. 2019. Industry-environment system management based on an uncertain Gaussian diffusion optimization model for coal-dependent cities in ecologically fragile areas. *Journal of Cleaner Production* **234**:832–857 DOI 10.1016/j.jclepro.2019.06.142.